

# Effects of bottom topography on the spin-up in a cylinder

**Journal Article****Author(s):**

Burmann, Fabian; Noir, Jérôme

**Publication date:**

2018

**Permanent link:**

<https://doi.org/10.3929/ethz-b-000293953>

**Rights / license:**

[Creative Commons Attribution 4.0 International](#)

**Originally published in:**

Physics of Fluids 30(10), <https://doi.org/10.1063/1.5051111>

# Effects of bottom topography on the spin-up in a cylinder

Fabian Burmann, and Jerome Noir

Citation: [Physics of Fluids](#) **30**, 106601 (2018); doi: 10.1063/1.5051111

View online: <https://doi.org/10.1063/1.5051111>

View Table of Contents: <http://aip.scitation.org/toc/phf/30/10>

Published by the [American Institute of Physics](#)

---

---

**PHYSICS TODAY**

WHITEPAPERS

## ADVANCED LIGHT CURE ADHESIVES

Take a closer look at what these environmentally friendly adhesive systems can do

READ NOW

PRESENTED BY  
**MASTERBOND**  
ADHESIVES | SEALANTS | COATINGS

# Effects of bottom topography on the spin-up in a cylinder

Fabian Burmann<sup>a)</sup> and Jerome Noir

*Institute for Geophysics, ETH Zürich, Sonneggstrasse 5, 8092 Zurich, Switzerland*

(Received 6 August 2018; accepted 12 September 2018; published online 5 October 2018)

Motivated by better understanding the long-standing issue of the role of topography on the transport of angular momentum in rapidly rotating fluids, we conducted spin-up experiments in a straight cylinder with a regular pavement of rectangular blocks at the bottom. We perform particle image velocimetry measurements to monitor the decay of the initial differential motion generated by the sudden increase of the container rotation rate. We observe that the re-synchronization time, the so-called spin-up time, is shorter in the presence of topography with a minimum at a particular length scale of the topography pattern. We show evidence of energy transport by inertial waves as well as non-linear mechanisms leading to a scaling of the spin-up time significantly different from the classical  $E^{-1/2}$  in the absence of topography. © 2018 Author(s). All article content, except where otherwise noted, is licensed under a Creative Commons Attribution (CC BY) license (<http://creativecommons.org/licenses/by/4.0/>). <https://doi.org/10.1063/1.5051111>

## I. INTRODUCTION

Rapidly rotating flows are omnipresent in planetary dynamics, whether considering liquid cores, subsurface oceans, or gaseous atmospheres. The effects of topography on the flows in these liquid layers have been addressed mostly for stratified fluids such as the Earth's atmosphere and oceans, where internal waves play a fundamental role.<sup>1–6</sup> Less attention has been given to planetary core dynamics in the presence of topography, where most studies have been performed on the interplay between rotating convection and topography in different geometries. The case of a cylindrical annulus with a variable height on the top and bottom end walls has been investigated theoretically,<sup>7</sup> numerically,<sup>8,9</sup> and experimentally.<sup>10</sup> Even though they differ in the exact configurations, all models find the existence of thermal Rossby waves. In a more core-like geometry, Calkins *et al.*<sup>11</sup> numerically investigated the effect of a single Gaussian ridge penetrating the outer core, leading to a resonance of the zonal flow with a Rossby wave. However, the mechanism underlying the transport of energy and angular momentum from the scale of the topography to the large scale of the zonal flow or the small scales of local vortices have yet to be identified.

In the present study, we investigate experimentally the classical problem of the flow in a cylinder after a sudden increase of its rotation rate, the so-called spin-up. In this system, the rate at which the fluid synchronizes with the container gives a measure of the axial torque acting on the fluid and hence the coupling between the container and fluid. For the spin-up in the linear limit of a small increase of the rotation rate, it is now well established<sup>12–14</sup> that the characteristic time for the fluid to resynchronize with the container is proportional to  $L\Omega^{-1/2}\nu^{-1/2}$ , with  $L$  being the half height of the container,  $\Omega$  being the rotation rate, and  $\nu$  being the kinematic viscosity of the fluid. As the initial rapid change of the rotation rate is

increased, non-linear effects become significant. Detailed discussions on the non-linear spin-up are provided in the reviews of Benton and Clark<sup>15</sup> and Duck and Foster.<sup>16</sup> Both the linear spin-up and non-linear spin-up in a right cylinder with flat end walls have been extensively studied theoretically,<sup>17,18</sup> numerically,<sup>19</sup> and experimentally.<sup>20,21</sup>

The present study differs from the aforementioned literature as we add bottom topography to the spin-up problem, which we expect to inhibit the azimuthal circulation. This is the case in the spin-up in a tank with a sloping bottom, for which Pedlosky and Greenspan<sup>22</sup> developed an analytical solution. In the absence of the geostrophic flow, westward traveling Rossby waves are excited in the system, which decay on the same time scale as the flow in the flat bottom cylinder. The theoretical results for this setup were later validated experimentally and numerically by Van De Konijnenberg *et al.*,<sup>23</sup> who also report on vortex shedding in the system. Depending on the steepness of the sloping bottom in spin-up experiments in a rectangular container, Heijst *et al.*<sup>24</sup> observed either a reorganization into cyclonic and anticyclonic flow cells for small sloping angle or an irregular and unsteady flow pattern in the case of a steep angle. A more extreme bottom topography with no geostrophic contours is represented by the spin-up in a half cone studied by Li *et al.*<sup>25</sup> Van De Konijnenberg and Van Heijst<sup>26</sup> investigated the spin-up from rest in a rectangular domain with a piecewise flat topography. They reported the following three stages of the spin-up process. A first stage is characterized by an initial flow of uniform vorticity  $\chi = -2\Omega$ ; during the second stage, the flow field detaches from the container walls and a subsequent reorganization in to small scale vortices resembling both the structure of the container and the topography takes place. Finally, in the third stage, the motion in the experiment decays due to Ekman pumping in the bottom boundary layer. Despite lacking a quantitative measurement of the kinetic energy, they claim that the third stage happens only when the flow has already lost most of its kinetic energy.

<sup>a)</sup>fabian.burmann@erdw.ethz.ch

In contrast to Van De Konijnenberg and Van Heijst,<sup>26</sup> we impose a strong background rotation and perform experiments in the linear limit of a small increase in the rotation rate. We use particle image velocimetry (PIV) to investigate the temporal evolution of the flow field and the associated kinetic energy in spin-up experiments with a discontinuous bottom topography of different horizontal length scales.

## II. THEORY

We consider a homogeneous and incompressible fluid enclosed in a rapidly rotating straight cylinder. At time  $t = t_0$ , we suddenly increase the rate of rotation of the container and monitor in time the decay of the initial differential motion. Here, we compare the following two cases, first the cylinder has a flat top and bottom end wall and second the bottom of the tank is paved with blocks of different lateral extent (Fig. 1). The system is characterized by the initial rotation of the container  $\Omega_0$ , the small increase of the rotation rate  $\delta\Omega$ , the half height of the cylinder  $L$ , the radius  $R$ , and the length scale of the topography  $\lambda_s$ . We work under the assumption of an incompressible and homogeneous fluid of density  $\rho$  and kinematic viscosity  $\nu$ .

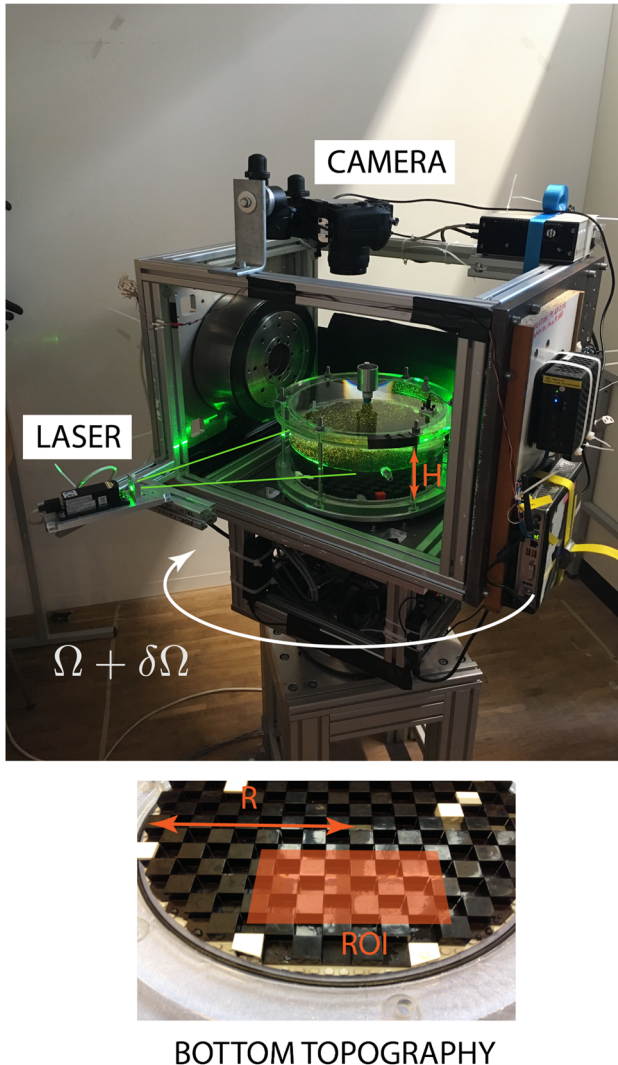


FIG. 1. Photograph of the experiment and the bottom topography.

The dynamics of the system are governed by the conservation of mass and momentum expressed in the frame attached to the container. Using  $\Omega_0^{-1}$  as a time scale,  $L$  as a length scale, and  $U = L\delta\Omega$  as a velocity scale, the non-dimensional Navier-Stokes equation is written as

$$\nabla \cdot \mathbf{u} = 0, \quad (1)$$

$$\partial_t \mathbf{u} + \varepsilon(\mathbf{u} \cdot \nabla) \mathbf{u} + 2\hat{\mathbf{z}} \times \mathbf{u} = -\nabla \pi + E \nabla^2 \mathbf{u}, \quad (2)$$

where  $\mathbf{u}$  is the velocity,  $\pi$  is the reduced pressure including centrifugal acceleration, and  $\hat{\mathbf{z}}$  is the axis of rotation. The two control parameters of the system are the Rossby number

$$\varepsilon = \delta\Omega/\Omega_0, \quad (3)$$

measuring the ratio between advection and Coriolis forces, and the Ekman number

$$E = \nu/\Omega_0 L^2, \quad (4)$$

which gives the ratio between viscous and Coriolis forces. In the limit of small  $E$  and small  $\varepsilon$ , the system supports inertial waves propagating with a group velocity expressed as

$$v_g = \frac{2}{|\mathbf{k}|^3} \mathbf{k} \times (\boldsymbol{\Omega}_0 \times \mathbf{k}), \quad (5)$$

where  $\mathbf{k}$  is the wave vector. In the limit of a quasi-steady perturbation, inertial waves propagate vertically giving rise to the so-called Taylor-Proudman columns.

In the case of a spin-up with flat end walls, the fluid interior and the container can exchange angular momentum only by viscous coupling through a viscous boundary layer of thickness  $L_{BL} = E^{1/2}L$ , the so-called Ekman layer, at the top and the bottom of the container. Fluid is sucked into this boundary layer where the angular momentum is exchanged with the container before being re-injected into the interior. This suction/injection mechanism gives rise to a recirculation in the bulk referred to as Ekman pumping. It leads to a typical time scale  $\tau = E^{-1/2}\Omega_0^{-1}$  for the fluid to be spun-up. For straight cylinder with flat end walls, the asymptotic limits  $\varepsilon \ll 1$  and  $E \ll 1$  yield a flow in the interior that remains primarily in the form of a solid body rotation

$$\mathbf{u}(s, \phi, z, t) = \delta\Omega(t) \times \mathbf{r} + \tilde{\mathbf{u}}(s, \phi, z, t), \quad (6)$$

where  $\tilde{\mathbf{u}} \propto E^{1/2}$  is the Ekman pumping in the interior. Both  $\delta\Omega(t) \times \mathbf{r}$  and  $\tilde{\mathbf{u}}$  decay exponentially in time with a decay rate

$$\sigma \sim E^{1/2}. \quad (7)$$

## III. EXPERIMENTAL SETUP AND DATA PROCESSING

We perform spin-up experiments in an acrylic straight cylinder of an equal height ( $H$ ) and radius ( $R$ ) of 142.5 mm that is mounted on a rotating table driven by a Yaskawa SGMCS-35E3B11 direct drive servomotor controlled by a SGDV-5R5A11A servopack to maintain the rotation rate at the desired value. The servopack is connected to a computer via an MP2300S interface. For the topography, we use a Prusa i3 3D printer to print a chessboard like arrangement of square blocks in the sizes  $8 \times 8$  mm,  $16 \times 16$  mm,  $32 \times 32$  mm, and  $64 \times 64$  mm, with a constant height of 16 mm, as shown in Fig. 1. Each topography is characterized by its dimensionless length scale  $\lambda_s$ , the ratio between the block size, and the radius  $R$  of



the cylindrical container. Although  $\lambda_s$  is the relevant physical quantity, it is more convenient to refer to a particular topography by using a nomenclature based on the absolute size of the blocks, namely, TOPO 16 for the  $16 \times 16$  mm, TOPO 32 for the  $32 \times 32$  mm, and so on.

To interrogate the flows in a vertical plane containing the axis of rotation, we adopt the well-known technique of direct visualisation with Kalliroscope rheoscopic fluid<sup>27</sup> and a vertical laser light sheet. From the images, we obtain qualitative information regarding the vertical structures developing in the system. In addition, we perform quantitative measurements of the velocity using Particle Image Velocimetry (PIV) techniques in three planes perpendicular to the rotation axis at  $z^* = 3$  cm, 7.5 cm, and 11 cm above the bottom surface,

corresponding to the dimensionless heights  $z = z^*/H = 0.21$ , 0.53, and 0.78. Movies are recorded with a Nikon<sup>TM</sup> D810 camera fixed on the turntable with a frame rate of 60 images per second at 2K resolution. Illumination is provided by a Spectra Physics Excelsior diode pumped CW-laser at a wavelength of 532 nm. To increase the contrast, we seed the fluid with fluorescent polyethylene microspheres (from Cospheric LLC) of diameter  $38 \mu\text{m}$ – $45 \mu\text{m}$  and density  $1.004 \text{ g cm}^{-3}$ . The absorption band of the particles extends from 300 nm to 550 nm, while the emission peaks at 600 nm. We use an optical narrow bandpass filter to reject the green excitation light, filtering out all reflections on the acrylic walls and thus increasing drastically the contrast of the images.

TABLE I. Characterization of the topography (nomenclature and non-dimensional length scale  $\lambda_s$ ) and mean spin-up time of repeated experiments  $\tau$ , together with standard deviation  $\tau_{SD}$ . The final row gives the exponent of the  $\tau = aE^b$  scaling for all topographies together with 95%-confidence interval.

E	$\varepsilon$	$z$	$\lambda_s = 0.06$ TOPO 8		$\lambda_s = 0.12$ TOPO 16		$\lambda_s = 0.24$ TOPO 32		$\lambda_s = 0.48$ TOPO 64		$\lambda_s = 1$ PLAIN		$E^{-1/2}$
			$\tau$	$\tau_{SD}$	$\tau$	$\tau_{SD}$	$\tau$	$\tau_{SD}$	$\tau$	$\tau_{SD}$	$\tau$	$\tau_{SD}$	
$5.40 \times 10^{-5}$	0.025	0.21	48.10	0.28	32.18	0.06	37.27	0.23	46.17	3.90			
$3.25 \times 10^{-4}$	0.05	0.21	44.17	0.33	26.65	0.20	22.77	0.06	27.44	0.17			
$1.62 \times 10^{-4}$	0.05	0.21	45.57	0.53	28.50	0.00	26.98	0.10	34.98	0.59			
$1.08 \times 10^{-4}$	0.05	0.21	46.80	0.04	30.02	0.03	29.66	0.07	39.71	0.86			
$8.12 \times 10^{-5}$	0.05	0.21	46.46	0.43	30.90	0.54	31.60	0.01	42.78	0.41			
$6.48 \times 10^{-5}$	0.05	0.21	46.32	0.02	29.77	1.87	32.68	0.06	45.32	0.44			
$5.40 \times 10^{-5}$	0.05	0.21	45.50	0.23	31.04	0.02	33.71	0.05	49.33	4.03			
$4.64 \times 10^{-5}$	0.05	0.21	44.92	0.34	31.37	0.13	34.69	0.02	48.42	1.49			
$4.08 \times 10^{-5}$	0.05	0.21	43.70	0.75	31.49	0.21	35.18	0.06	50.23	0.34			
$3.61 \times 10^{-5}$	0.05	0.21	42.95	0.00	30.09	0.06	34.36	0.39	48.62	1.12			
$5.40 \times 10^{-5}$	0.1	0.21	42.51	0.05	26.80	0.01	31.25	0.07	42.80	0.02			
$8.12 \times 10^{-5}$	0.025	0.53	48.54	0.09	29.93	0.22	36.28	0.27	48.52	1.16	119.76	0.82	110.97
$5.40 \times 10^{-5}$	0.025	0.53	49.41	0.11	31.99	0.21	40.55	0.24	57.68	0.58	151.03	1.17	135.91
$4.08 \times 10^{-5}$	0.025	0.53	49.99	0.51	32.97	0.25	43.36	0.38	65.70	0.10	174.77	1.15	156.94
$3.25 \times 10^{-4}$	0.05	0.53	41.10	0.40	24.51	0.08	23.52	0.39	29.71	0.10	61.00	0.48	55.49
$1.62 \times 10^{-4}$	0.05	0.53	45.16	0.16	27.04	0.24	27.58	0.17	35.70	0.09	88.04	0.73	78.47
$1.08 \times 10^{-4}$	0.05	0.53	47.41	0.27	29.16	0.09	31.07	0.20	41.57	0.25	107.64	0.77	96.11
$8.12 \times 10^{-5}$	0.05	0.53	47.87	0.10	30.09	0.06	32.96	0.09	44.74	0.21	123.81	0.66	110.97
$6.48 \times 10^{-5}$	0.05	0.53	47.61	0.14	30.98	0.09	34.79	0.11	48.08	0.43	138.24	0.30	124.07
$5.40 \times 10^{-5}$	0.05	0.53	46.34	0.08	31.27	0.11	35.50	0.14	48.66	1.17	149.09	0.94	135.91
$4.64 \times 10^{-5}$	0.05	0.53	45.83	0.27	31.75	0.20	36.20	0.49	51.23	0.48	157.86	1.45	146.80
$4.08 \times 10^{-5}$	0.05	0.53	44.98	0.48	31.79	0.23	36.90	0.24	53.14	1.24	162.42	1.51	156.94
$3.61 \times 10^{-5}$	0.05	0.53	44.45	0.35	31.84	0.15	37.72	0.20	53.63	0.34	170.41	2.19	166.46
$8.12 \times 10^{-5}$	0.1	0.53	43.65	0.48	26.78	0.06	30.40	0.09	39.61	0.25	114.77	5.40	110.97
$5.40 \times 10^{-5}$	0.1	0.53	43.42	0.07	26.90	0.10	31.59	0.12	42.88	0.18	138.73	0.61	135.91
$4.08 \times 10^{-5}$	0.1	0.53	44.03	0.06	27.76	0.14	33.23	0.72	45.67	0.21	160.66	0.73	156.94
$5.40 \times 10^{-5}$	0.025	0.78	49.07	0.38	33.68	0.13	43.15	0.02	57.79	1.38			
$3.25 \times 10^{-4}$	0.05	0.78	40.67	0.19	23.89	0.32	24.44	0.77	26.36	0.94			
$1.62 \times 10^{-4}$	0.05	0.78	43.79	0.11	26.58	0.10	29.80	0.22	31.59	0.20			
$1.08 \times 10^{-4}$	0.05	0.78	45.56	0.27	29.00	0.13	33.19	0.25	37.89	0.54			
$8.12 \times 10^{-5}$	0.05	0.78	42.62	0.33	30.29	0.04	35.41	0.09	42.80	0.64			
$6.48 \times 10^{-5}$	0.05	0.78	45.98	0.02	31.43	0.13	37.43	0.05	46.39	0.61			
$5.40 \times 10^{-5}$	0.05	0.78	44.97	0.13	31.94	0.11	38.64	0.21	50.76	0.22			
$4.64 \times 10^{-5}$	0.05	0.78	44.66	0.24	32.94	0.10	40.04	0.28	53.66	0.76			
$4.08 \times 10^{-5}$	0.05	0.78	44.13	0.11	33.57	0.02	41.29	0.06	59.73	0.25			
$3.61 \times 10^{-6}$	0.05	0.78	43.35	0.19	34.27	0.02	41.87	0.39	62.62	0.34			
$5.40 \times 10^{-5}$	0.1	0.78	42.35	0.05	26.36	0.04	32.54	0.28	39.97	0.10			
E scaling exponent			$-0.02 \pm 0.04$		$-0.12 \pm 0.02$		$-0.21 \pm 0.02$		$-0.30 \pm 0.02$		$-0.45 \pm 0.04$		

From the videos, we extract individual frames and adopt a contrast limited adaptive histogram equalization (CLAHE) algorithm to optimize the individual frames. We use the same mask on all movie frames to select a Region Of Interest (ROI) of size  $12.5 \times 8.2$  cm, and each frame is processed using DPIV-soft2010<sup>28</sup> to extract 60 velocity fields per second made of  $41 \times 34$  vectors. From the velocity fields, we extract the mean kinetic energy over the entire ROI and maps of the vorticity.

We apply the same experimental protocol for all experiments. The table is set into rotation at  $\Omega_0$ , and we wait until any visible motion in the cylinder has ceased. We start recording videos of the fluid in the container 5 s before we increase the rotation rate of the table to  $\Omega_0 + \delta\Omega$  and record videos for about 3 min. The increase of the table rotation to  $\Omega_0 + \delta\Omega$  happens within 0.2 s, but oscillations around  $\Omega_0 + \delta\Omega$  remain present for around 2 s. At all three heights, we perform experiments at nine different rotation rates, linearly distributed between  $0.628 \text{ rad s}^{-1}$  and  $5.655 \text{ rad s}^{-1}$ , corresponding to the Ekman numbers between  $3.25 \times 10^{-4}$  and  $5.4 \times 10^{-5}$ . For all experiments, we consider Rossby numbers of 0.05. In the midplane ( $z = 0.53$ ), we perform additional experiments at three Ekman numbers  $8.12 \times 10^{-5}$ ,  $5.40 \times 10^{-5}$ , and  $4.08 \times 10^{-5}$  at Rossby numbers 0.025 and 0.1. In the bottom plane ( $z = 0.21$ ) and top plane ( $z = 0.78$ ), additional experiments at Rossby numbers 0.025 and 0.1 are performed at one fixed Ekman number  $5.40 \times 10^{-5}$ . An overview of all performed experiments is provided in Table I.

## IV. RESULTS

### A. Spin-up time as a function of the length scale of the topography

In Fig. 2, we show the typical time evolution of the mean kinetic energy  $E_k = \langle \mathbf{u}^2 + \mathbf{v}^2 \rangle$ , where  $\langle \rangle$  denotes the space average, deduced from the PIV measurements in the mid plane at  $z = 0.53$ . We present the time series for five different topography length scales [ $\lambda_s = 0.06$  (TOPO 08),  $0.12$  (TOPO 16),  $0.24$  (TOPO 32),  $0.48$  (TOPO 64), as well as the spin

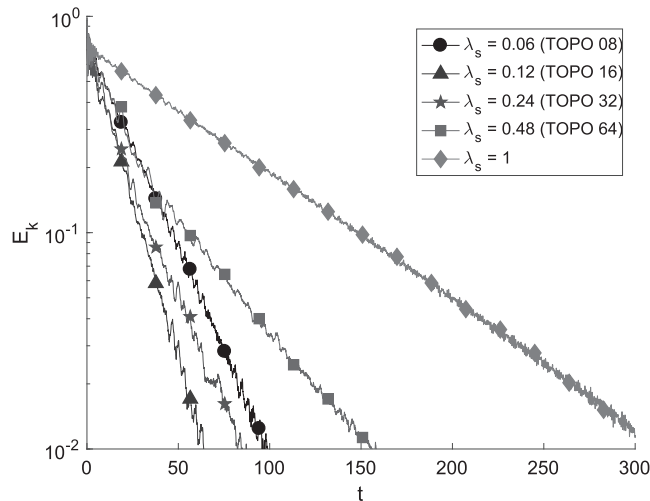


FIG. 2. Time series of the mean kinetic energy during the spin-up for different topographies recorded in the mid plane ( $z = 0.53$ ) at  $\varepsilon = 0.05$  and  $E = 5.40 \times 10^{-5}$ .

up with a flat bottom  $\lambda_s = 1$ ], and the Rossby number and Ekman number are fixed to  $\varepsilon = 0.05$  and  $E = 5.40 \times 10^{-5}$ , respectively.

In all experiments, the time evolution is characterized by an exponential decay with an e-folding time that depends on the topography. With the exception of  $\lambda_s = 0.48$ , where we observe a change in the logarithmic slope for late stages of the spin-up, we observe the same decay rate over the whole measurement time.

We first extract the decay rate  $\sigma$  of the kinetic energy from the time series, by picking the initial spin-up time  $t_0$  and the initial kinetic energy  $E_0$  and applying a nonlinear least square algorithm to fit an exponential function,

$$E_k = E_0 \exp[-\sigma(t - t_0)]. \quad (8)$$

We define the spin-up time as  $\tau = 2/\sigma$ . The experimental values of  $\tau$  for all  $E$  and  $\varepsilon$  are reported in Table I for each topography, where the uncertainties  $\tau_{SD}$  are obtained by performing multiple experiments with the same parameters.

The spin-up time  $\tau$  as a function of  $\lambda_s$  is shown in Fig. 3 in the three different planes at  $z = 0.21$ ,  $0.53$ , and  $0.78$  above the bottom, where the Ekman number is fixed at  $E = 5.40 \times 10^{-5}$  and three Rossby numbers  $\varepsilon = 0.025$ ,  $0.05$ , and  $0.1$  are displayed. Additionally, we display the theoretical spin-up time

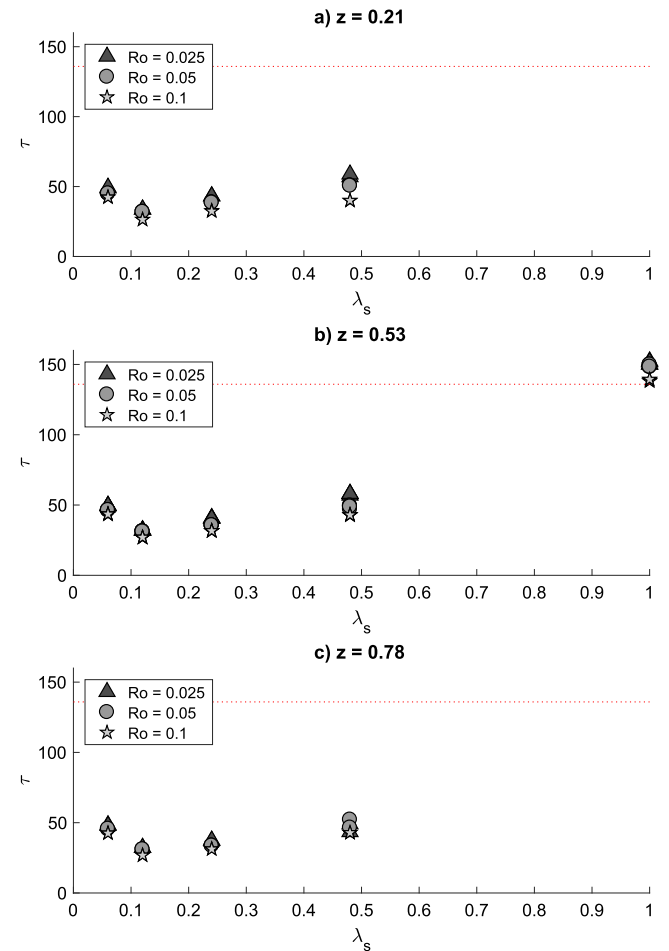


FIG. 3. Spin-up time as a function of topography wavelength  $\lambda_s$  in experiments at the Ekman number  $E = 5.40 \times 10^{-5}$  and Rossby numbers  $\varepsilon = 0.025$ ,  $0.05$ , and  $0.1$ . The red line indicates the theoretical spin-up time for a flat cylinder.

for a cylinder with a flat bottom. In all cases, we observe that introducing topography enhances the spin-up process resulting in a shorter spin-up time. The spin-up times in different measurement planes are not identical, but we do not find a systematic dependence of the spin-up time on the altitude of the measurement. Regarding the Rossby number, we find a decrease of the spin-up time with increasing Rossby number, indicating that the finite Rossby number might still have an effect on the dynamics in the system. However, the most striking finding is that one particular length scale  $\lambda_s = 0.12$  (TOPO 16) minimizes the spin-up time for all  $\varepsilon$  at all levels, which holds at all other Ekman numbers but the largest one,  $E \sim 10^{-4}$ , for which the spin-up time for  $\lambda_s = 0.12$  (TOPO 16) and  $\lambda_s = 0.24$  (TOPO 32) is indistinguishable from one another. The existence of a particular wavelength minimizing the spin-up time is not totally surprising. Indeed, the two end cases  $\lambda_s = 1$  and  $\lambda_s = 0$  correspond to a flat cylinder and should result in the same spin-up time. If intermediate topography has a positive or negative effect, we expect a critical wavelength at which it is maximum or minimum, respectively.

## B. Spin-up time as a function of the Ekman number

Considering a fixed Rossby number  $\varepsilon = 0.05$ , small enough for the flow to remain laminar over the entire range of accessible Ekman numbers, we investigate how the spin-up time varies with  $E$  for various topographies (Fig. 4). In all cases, we assume a scaling of the spin-up time  $\tau = aE^{-b}$  represented by the red dashed lines, where  $a$  and  $b$  are estimated by a non-linear least square inversion. For the cylinder without topography, we recover the well-established scaling law  $\tau \propto E^{-1/2}$ . In all experiments with topography, we observe a significant deviation from this laminar scaling with the largest discrepancy obtained for  $\lambda_s = 0.06$  (TOPO 08), with a spin-up time at all altitudes almost independent of the Ekman number. For topography with  $\lambda_s > 0.06$ , we observe a scaling law exponent  $b$  increasing with  $\lambda_s$  but always significantly smaller than  $1/2$ . We notice a slight inflection at the lowest Ekman numbers, which may suggest that we are not yet in a fully asymptotic regime. Of particular interest is the case of  $\lambda_s = 0.06$  (TOPO 08), where the spin-up time becomes almost independent of

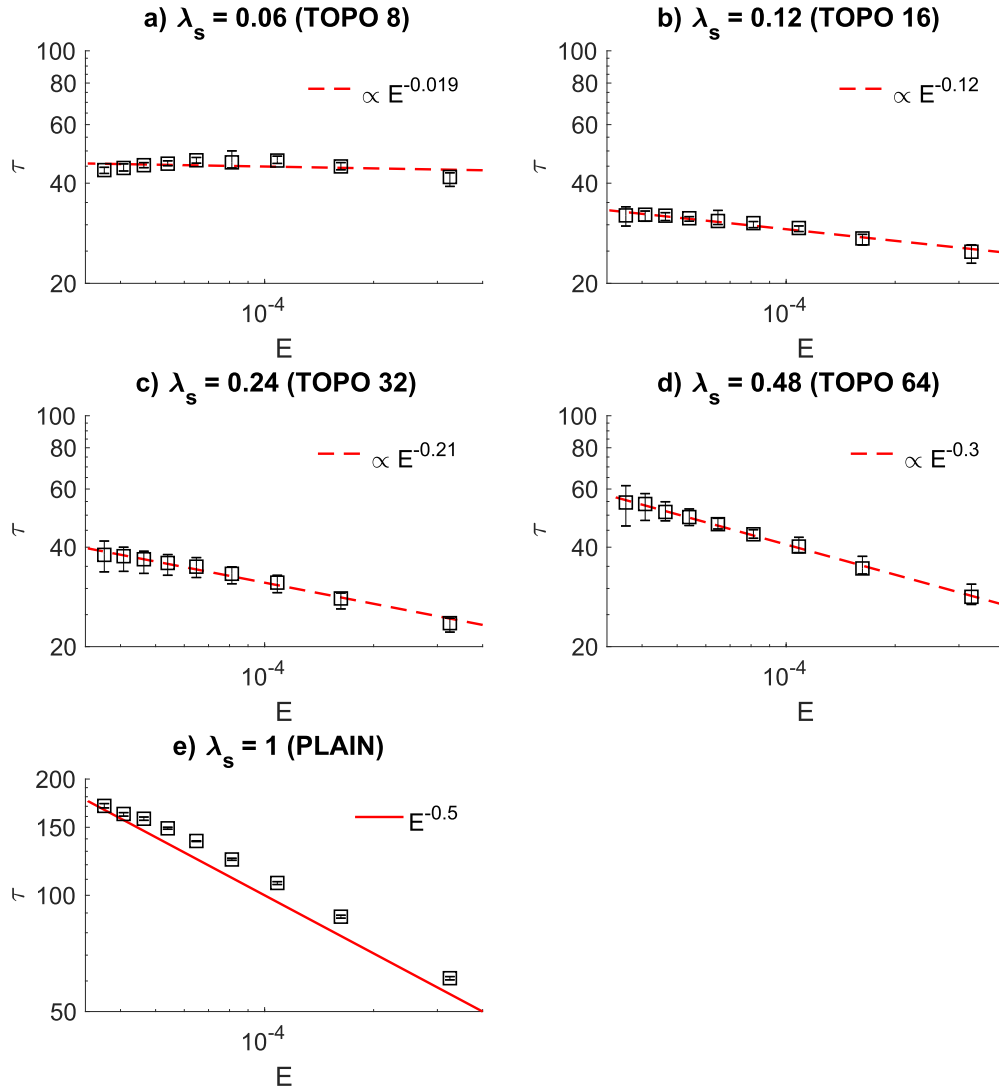


FIG. 4. Spin-up time as a function of the Ekman number  $E$  for different topography in spin-up experiments at a Rossby number of 0.05. Dashed red lines in panels (a)–(d) give the best fitting power law of the form  $\tau = aE^b$ . Solid red line in panel (e) gives the theoretical spin-up time  $\tau = E^{-1/2}$ . The error bars correspond to the minimum and maximum values measured in the three PIV planes ( $z = 0.21, 0.53$ , and  $0.78$ ).

the Ekman number, usually the signature of non-linear effects dominating energy and angular momentum transport.

### C. Flow structure

To infer the structure and dynamics of the flow in our experiments, we use the PIV velocity fields to reconstruct time-resolved 2D maps of the axial vorticity  $\chi = \partial u/\partial y - \partial v/\partial x$  and streamlines in three different horizontal planes at  $z = 0.21$ ,  $0.53$ , and  $0.78$ . In addition, we use Kalliroscope rheoscopic fluid and a vertical light sheet to visualize shear structures in a meridional plane.

We observe an initial phase with a flow in the form of a solid body rotation with a mean vorticity  $-2\delta\Omega$ . Shortly after

this initial phase, the velocity field exhibits patterns reflecting the length scale of the bottom topography as illustrated in Fig. 5, where each row corresponds to one length scale of the bottom topography  $\lambda_s$ , the left column displays the axial vorticity, averaged over  $\sim 0.6$  rotation times, and the right column displays streamlines. The snapshots are taken at  $t = 15.7$  after the spin-up started. The streamlines are superimposed on the pattern of the topography, where the grey squares represent the elevated sections. The typical time for the topography to reflect in the flow at a given altitude depends on  $\lambda_s$ , the larger it is, the sooner the structures can be observed. Indeed at  $t = 15.7$ , for the smallest topography  $\lambda_s = 0.06$  (TOPO 08), the streamlines still represent a solid body rotation, while larger topographies already show a significant departure from this

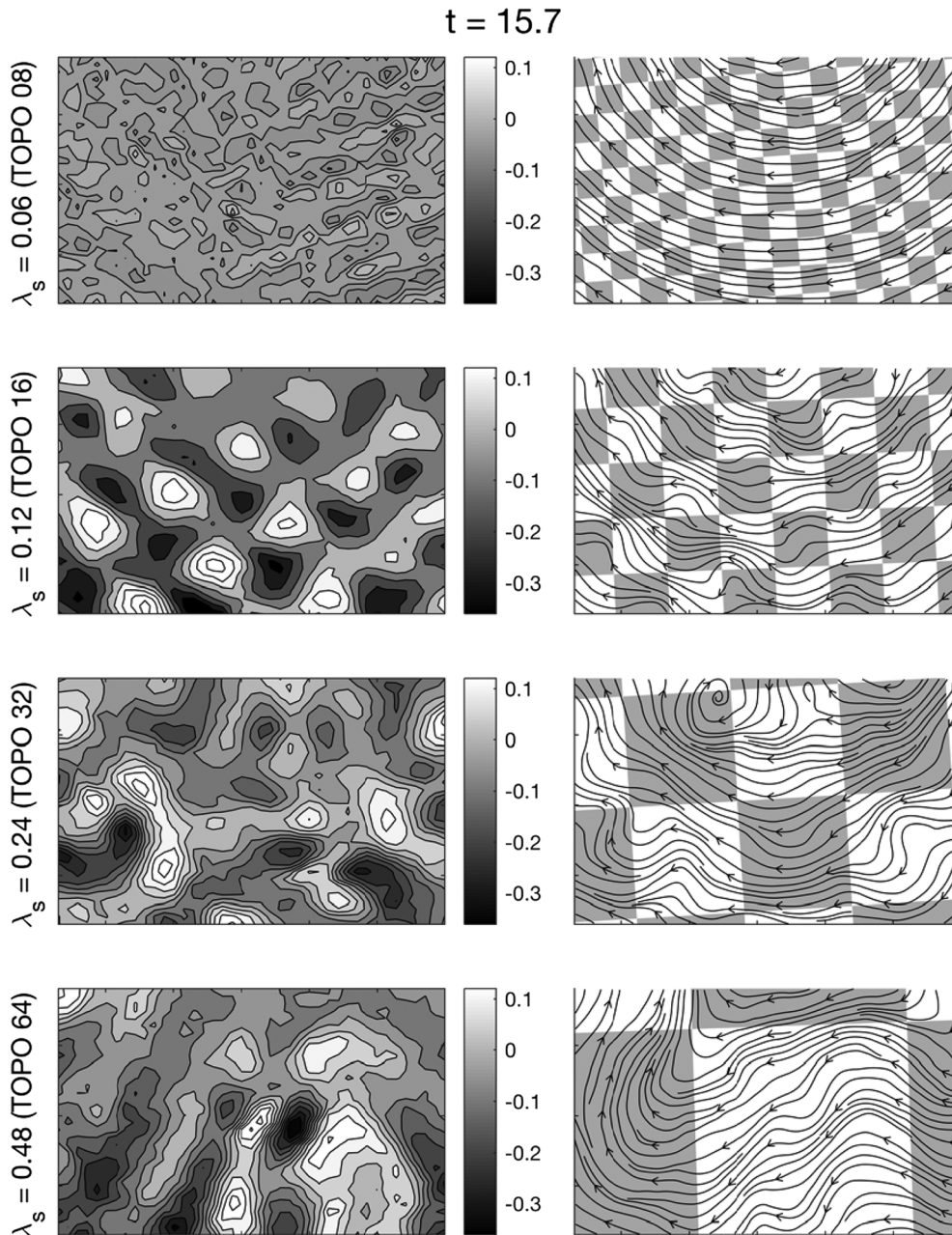


FIG. 5. Vorticity (left) and streamlines (right) measured in the mid plane ( $z = 0.53$ ) at a time of  $t = 15.7$  after the increase of the rotation rate. Grey color marks the elevated sections of the topography. The experimental conditions are  $\varepsilon = 0.05$  and  $E = 5.40 \times 10^{-5}$ . Dimensionless size of the ROI  $0.88 \times 0.55$ .



state with a non-zonal global circulation pattern. As the flow evolves with time, the global circulation becomes less relevant for the largest topography  $\lambda_s = 0.48$  (TOPO 64), while it remains a dominant feature at the smallest topography as illustrated in Fig. 6, which is the same as Fig. 5 but at  $t = 100.5$ . For  $\lambda_s = 0.48$  (TOPO 64), the flow is organized in vortices following the contours of the topography. Cyclonic vortices form in the low sections (white squares) of the topography and anticyclonic vortices form in the elevated sections (gray squares) in agreement with conservation of potential vorticity as observed by Van De Konijnenberg and Van Heijst.<sup>26</sup> For intermediate topographies, we observe a mixture of global circulation and vortical structures with cyclonic vortices in the low sections still observable at  $\lambda_s = 0.24$  (TOPO 32). This observation seems to hold at in particular at later times as

the intensity of the flow vanishes. Although present in the PIV field, the small perturbations at the scale of the smallest topography,  $\lambda_s = 0.06$  (TOPO 08), never dominate the flow at  $z = 0.53$ .

The alignment of the vortices with the topography at  $t = 100.5$  for  $\lambda = 0.48$  (TOPO 64) strongly suggests that the flow is geostrophic at this stage. We use Kalliroscope rheoscopic fluid and a vertical laser sheet to ascertain the structure of the flow in the direction parallel to the rotation axis. In Fig. 7, we present photographs of a meridional illuminated cross section, where the transition from bright to dark regions marks the presence of shear layers in the system. The experiments have been conducted at  $E = 5.40 \times 10^{-5}$  and  $\varepsilon = 0.05$ . Displayed are the three different topographies  $\lambda_s = 0.06$  (TOPO 08),  $\lambda_s = 0.12$  (TOPO 16), and  $\lambda_s = 0.24$  (TOPO 32)

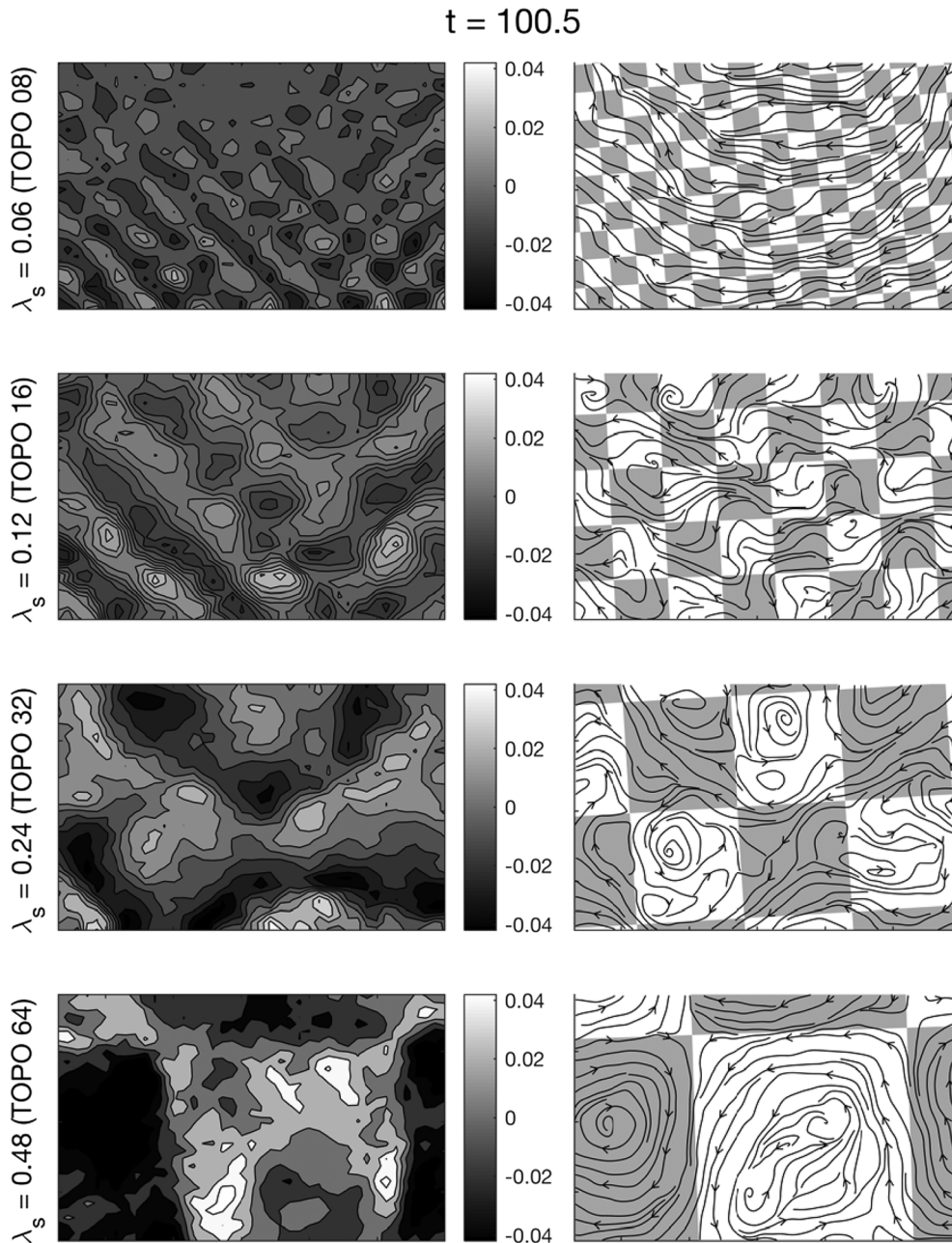


FIG. 6. Vorticity (left) and streamlines (right) measured in the mid plane ( $z = 0.53$ ) at a time of  $t = 100.5$  after the increase of the rotation rate. Grey color marks the elevated sections of the topography. The experimental conditions are  $\varepsilon = 0.05$  and  $E = 5.40 \times 10^{-5}$ . Dimensionless size of the ROI  $0.88 \times 0.55$ .



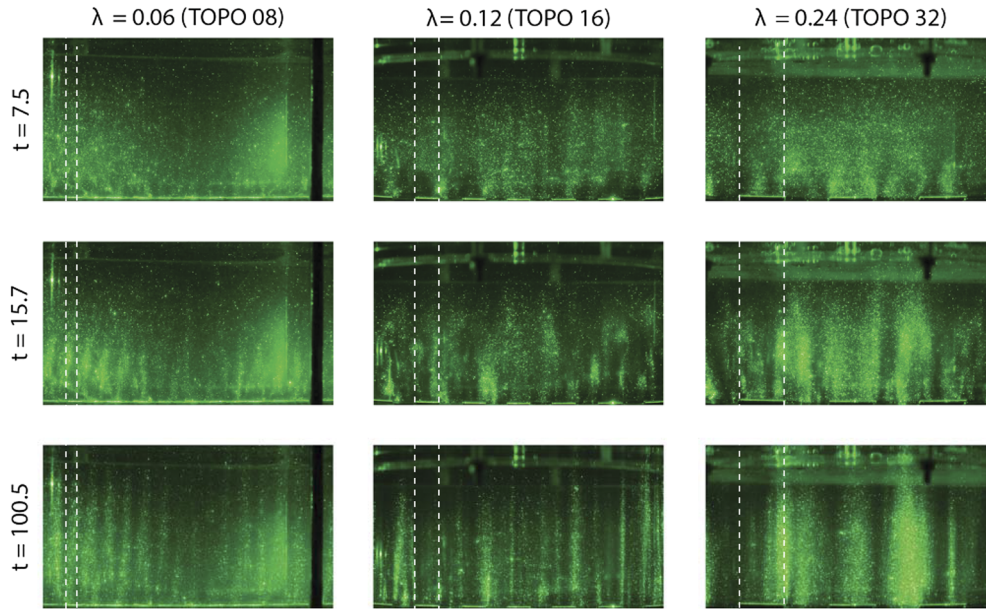


FIG. 7. Kalliroscope visualization of vertical shear layers in the fluid; the edges of one block of the topography are indicated by the vertical white dashed lines.  $E = 5.40 \times 10^{-5}$  and Rossby number 0.05.

at three times  $t = 7.5$ ,  $15.7$ , and  $100.5$ , the latest two corresponding to the vorticity fields and streamlines depicted in Figs. 5 and 6, respectively. In all experiments, small structures occur in the vicinity of the topography edges immediately after the spin-up of the tank, as shown in Fig. 7 at  $t = 7.5$ . As time evolves, these structures propagate upwards in agreement with the observation of vorticity patterns reported in Figs. 5 and 6, eventually becoming quasi-geostrophic as observed for  $t \sim 100.5$ . Since Kalliroscope is insensitive to global rotation, it is a powerful technique to emphasize localized shear that would otherwise be invisible using PIV. In particular, we note that for  $\lambda_s = 0.12$  (TOPO 16) and  $\lambda_s = 0.24$  (TOPO 32) at  $t = 100.5$ , structures do extend vertically in the fluid interior, suggesting that the second order fluctuations superimposed to the large scale circulation reported in Fig. 6 are quasi-geostrophic. Eventually, the structures fade out as the fluid resynchronizes with the cylindrical cavity, but they remain present for much longer than one e-folding time of the kinetic energy.

#### D. Inertial wave propagation

The Kalliroscope observations show quasi-geostrophic columns with a horizontal extent reflecting to the length scale of the bottom topography  $\lambda_s$  that might be formed by vertical propagation of inertial waves, which after several reflections form quasi-geostrophic columns. We also expect the sharp edges to spawn inertial waves in the system with a broad range of length scales  $\lambda < \lambda_s$ . Using the group velocity for a vertically traveling wave with a horizontal wave number  $k$ ,

$$|V_g(k)| = \frac{2\Omega_0}{|k|}, \quad (9)$$

we can derive a time of arrival  $t$  for each  $k$  and altitude  $z$  as

$$t(z, k) = \frac{z|k|}{2\Omega_0}. \quad (10)$$

To characterize the propagation of inertial waves, we calculate spectrograms of the axial vorticity in the three different PIV planes, i.e., the spatial Fourier transform of the vorticity as a function of the wave number  $k = \sqrt{k_x^2 + k_y^2}$  for each frame. Here  $k_x$  and  $k_y$  refer to the wave numbers of our square block topography in the direction of  $x$  and  $y$ , both as  $\pi/\lambda_s$ . The results are shown in Figs. 8 and 9, where the solid white line represents the theoretical time of arrival given by Eq. (10), the dashed white line represents the wave number of the topography  $k_s = \sqrt{2}\pi/\lambda_s$ , and the red dashed line represents a theoretical upper bound that will be introduced later in this section. We use the same color scale for all plots. Figure 8 shows the results for the two largest topographies  $\lambda_s = 0.24$  (TOPO 32) and  $\lambda_s = 0.48$  (TOPO 64), clearly exhibiting inertial wave packets propagating from the bottom to the top of the cylinder in agreement with Eq. (10). In addition, we observe that there is an upper bound on the wave number  $[k_{\max}(z)]$  for the inertial waves propagating in the system, that depends on the height of the measurement  $z$  but not on the length scale of the bottom topography. From Figs. 8 and 9 we obtain an estimate for  $k_{\max}(z)$  as  $k_{\max}(0.21) \sim 9$ ,  $k_{\max}(0.53) \sim 7$ , and  $k_{\max}(0.78) \sim 5$ . The limited extent of the ROI does not allow us to extract information for wave numbers less than  $k \sim 3$ , which for  $\lambda_s = 0.48$  (TOPO 64) is more than the topography wave number  $k_{64} = 1.6$ . In all the presented results, we should bear in mind that large scale circulation may not be captured by our spectrogram.

Figure 9 is the same as Fig. 8 but for  $\lambda_s = 0.06$  (TOPO 08) and  $\lambda_s = 0.12$  (TOPO 16). For  $\lambda_s = 0.12$  (TOPO 16), we still observe a vertical propagation with an arrival time in agreement with Eq. (10) and additionally the limitation on the large wave numbers seems to be in agreement with the thresholds observed for  $\lambda_s = 0.24$  (TOPO 32) and  $\lambda_s = 0.48$ . This is in contrast to  $\lambda_s = 0.06$  (TOPO 08), where only a marginal signature of the topography wave number is visible in the bottom

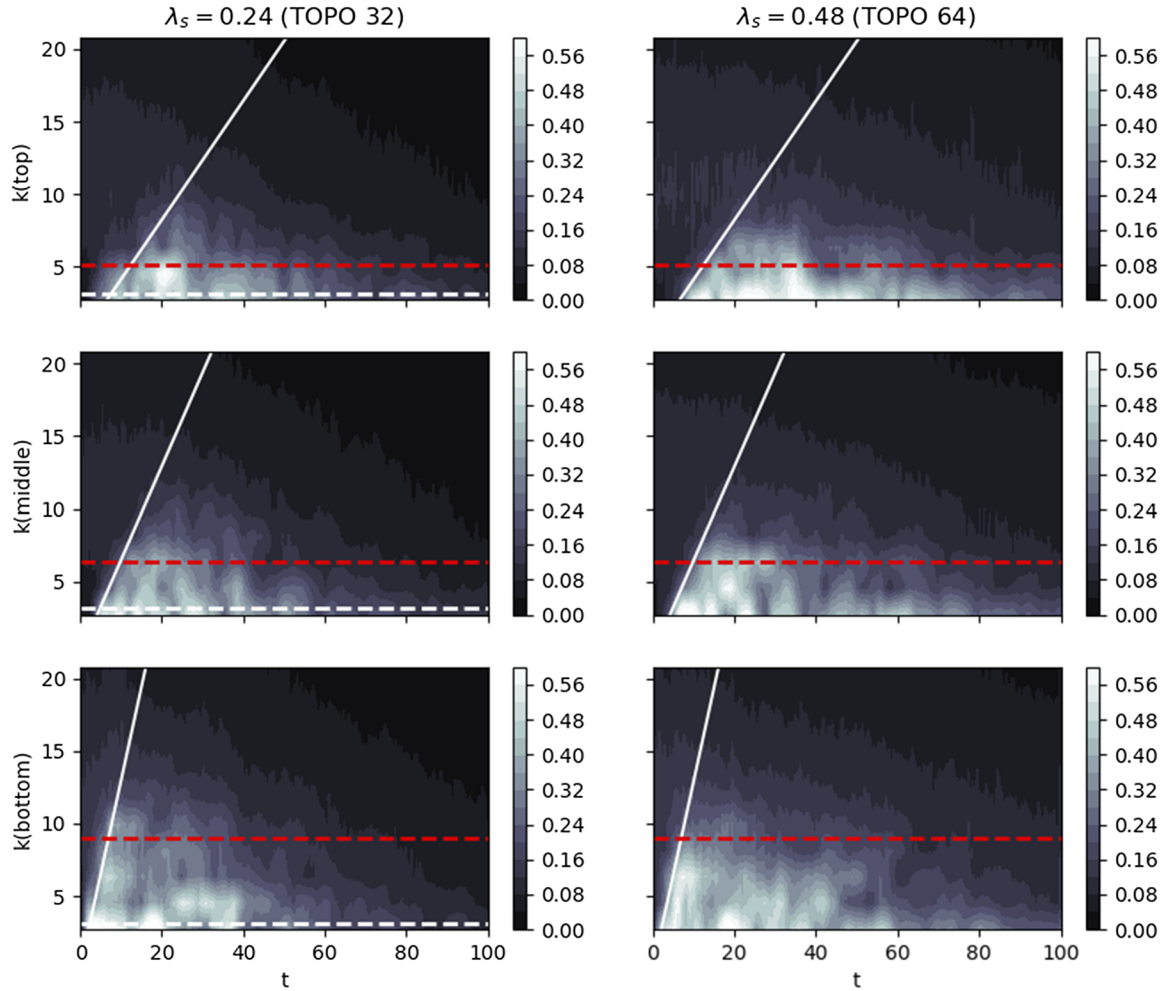


FIG. 8. Spectrogram of the axial vorticity: Left and right columns correspond to the topography  $\lambda_s = 0.24$  (TOPO 32) and  $\lambda_s = 0.48$  (TOPO 64), respectively. The three rows represent the plane of measurement,  $z = 0.21$ ,  $z = 0.53$ , and  $z = 0.78$  from the bottom to top. The white solid line corresponds to the theoretical prediction given by Eq. (10); the dashed white line corresponds to the wave number of the topography  $k_s$ . Finally the dashed red lines represent the upper bounds of the wave numbers that can propagate up to the different altitudes of the PIV planes according to Eq. (11). The experimental conditions are  $E = 5.40 \times 10^{-5}$  and  $Ro = 0.05$ , and all quantities are non-dimensional.

plane ( $z = 0.21$ ) with a time of arrival not compatible with inertial wave propagation. In the mid and top plane, the signal is barely detectable. For this topography, even at the altitude of the bottom plane, the topography wave number, presumably the smallest one to be excited, is significantly larger than  $k_{max}$ , as observed in each plane. The dimensionless vorticity is of the same order  $\varepsilon$  for  $\lambda_s = 0.12$  (TOPO 16),  $\lambda_s = 0.24$  (TOPO 32), and  $\lambda_s = 0.48$  (TOPO 64) but significantly smaller for  $\lambda_s = 0.06$  (TOPO 08). Meanwhile the PIV deduced streamlines for  $\lambda_s = 0.06$  (TOPO 08) clearly show that the flow remains in the form of a large scale circulation. However, these observations are not contradictory since scales of order one cannot be properly captured by the spectrogram; thus, low vorticity does not necessarily mean that energy has already been dissipated but that it may be on wave numbers below  $k \sim 3$ .

Two mechanisms may be responsible for the reported cutoff in wave numbers, viscous dissipation in the bulk or non-linear effects transferring energy across the spectrum faster than the waves propagating upward. The first mechanism is characterized by the viscous attenuation rates of inertial waves that propagate in the fluid,<sup>29</sup>  $1/\tau_{bulk} = 2k^2E$ , resulting in short

wavelengths being more dissipative. An order of magnitude of the cutoff wave number  $k_{max}$  in each plane can be obtained by comparing the decay time  $\tau_{bulk}$  to the travel time of the inertial waves (10). For bulk viscous dissipation, the upper bound in each plane would be  $k_{max} = 69, 52$ , and  $45$  for the bottom, mid, and top planes, respectively, much too large compared to the experimental cutoff around  $k_{max} \sim 5-9$ .

Meanwhile, Kolvin *et al.*<sup>30</sup> showed experimentally that two time scales control the transfer of energy in a rapidly rotating system,  $\tau_1(z, k) = z/v_g(k)$ , characterizing the transport of energy by inertial waves up to a distance  $z$  and  $1/\tau_2(k) \sim u_{rms}k$  the rate at which energy is transferred across the scales in the spectrum by non-linear effects. For  $\tau_1 < \tau_2$ , inertial waves transport energy faster than it spreads across the scales, while for  $\tau_1 > \tau_2$  the transfer across the spectrum dominates; hence, inertial waves do not propagate anymore. Using the initial differential rotation as a proxy for  $u_{rms}$ , the typical time scale characterizing the transfer across the spectrum is given by  $\tau_2 \sim (\varepsilon k)^{-1}$ , while the typical travel time of inertial waves to an altitude  $z$  in dimensionless units is written as  $\tau_1 = zk$  [see Eq. (10)]. Hence for each PIV plane, we can derive a maximum

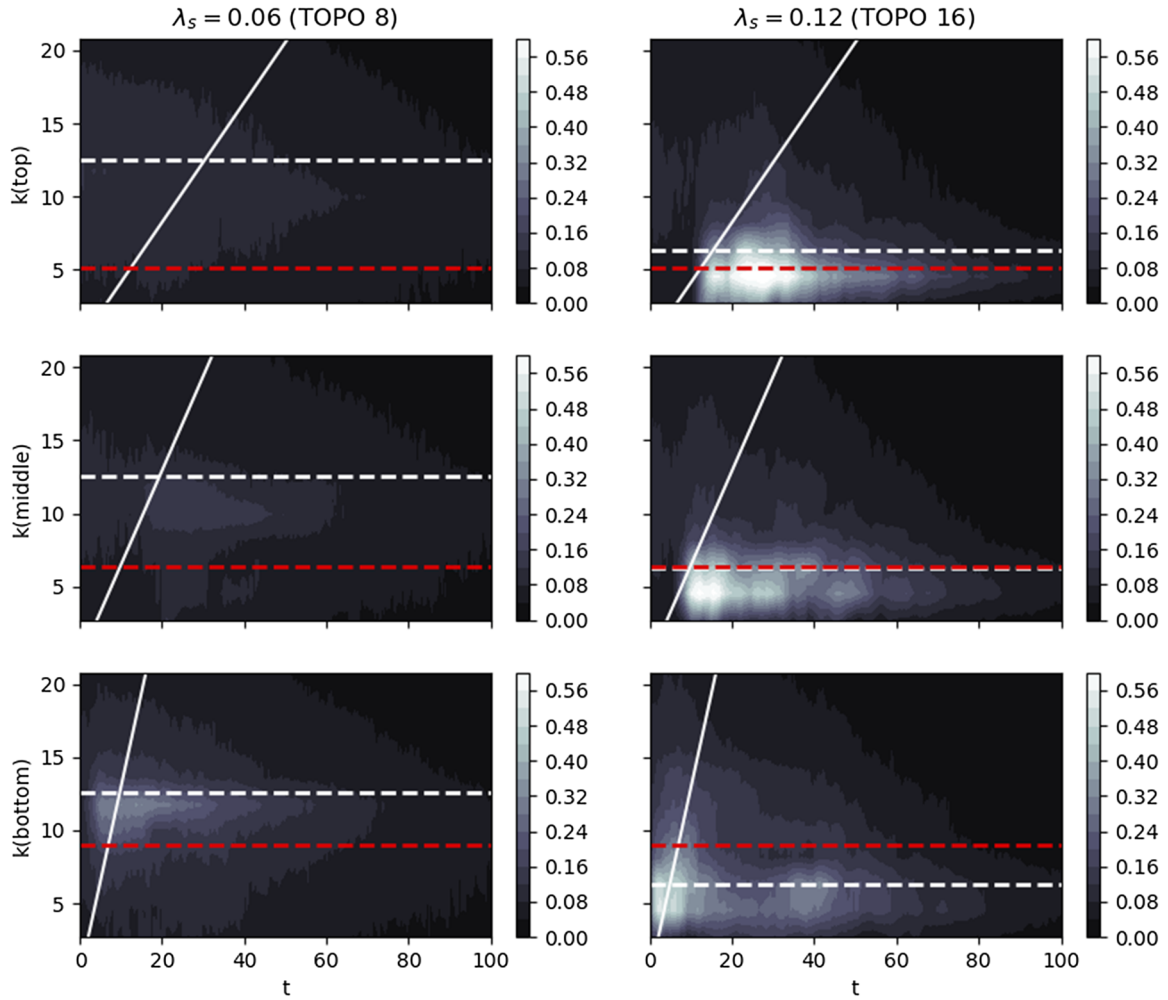


FIG. 9. Spectrogram of the axial vorticity: Left and right columns correspond to the topography  $\lambda_s = 0.06$  (TOPO 8) and  $\lambda_s = 0.12$  (TOPO 16), respectively. The three rows represent the plane of measurement,  $z = 0.21$ ,  $z = 0.53$ , and  $z = 0.78$  from the topography from bottom to top. The white solid line corresponds to the theoretical prediction given by Eq. (10); the dashed line corresponds to the wave number of the topography  $k_s$ . Finally the dashed red lines represent the upper bounds of the wave numbers that can propagate up to the different altitudes of the PIV planes according to Eq. (11). The experimental conditions are  $E = 5.40 \times 10^{-5}$  and  $Ro = 0.05$ , and all quantities are non-dimensional.

wave number above which the transfer across scales operates faster than upward transport by inertial waves,

$$k_{max} = \sqrt{\frac{1}{z\varepsilon}}. \quad (11)$$

It yields  $k_{max} = 9, 6$ , and  $4.5$  for the bottom, mid, and top plane, respectively. These values are reported as the red dashed line for each PIV plane in Figs. 8 and 9. The predicted cutoff wave numbers are in quantitative agreement with our observations; hence, there is little energy carried upward by inertial waves with  $k > k_{max}$ . For  $\lambda_s = 0.24$  (TOPO 32) and  $\lambda_s = 0.48$  (TOPO 64), the typical wave number of the topography is below the critical value  $k_{max}$  for all  $\varepsilon$  considered in this study. Hence for  $k_s < k_{max}(z)$ , inertial wave propagation dominates the transfer of energy in the system from the very beginning of the spin-up, while the non-linear mechanisms govern the energy transfer for  $k > k_{max}(z)$ , mostly affecting inertial waves spawned by the edges of the topography. This is in agreement with our streamlines representation in Figs. 5 and 6, where the signature of the bottom topography is particularly clear for  $\lambda_s = 0.24$  (TOPO 32) and  $\lambda_s = 0.48$  (TOPO 64). For

$\lambda_s = 0.12$  (TOPO 16) and  $\lambda_s = 0.06$  (TOPO 08), a comparison with the findings of Kolvin *et al.*<sup>30</sup> predicts significant non-linear effects to alter the propagation of inertial wave on the length scale of the topography especially in the upper half of the tank, which is supported both by our spectrograms and by the PIV derived streamlines. Nevertheless, it should be noted that our choice of  $U_{rms} \sim \varepsilon$  is only reasonable at the beginning of the spin-up before the differential velocity has decayed significantly. Once the differential velocity reduces, the non-linear effects will become less preponderant and inertial waves can again transit through the entire volume of fluid, which is supported by our Kalliroscope images showing that even for  $\lambda_s = 0.06$  (TOPO 08), waves on the length scale of the topography propagate and eventually form quasi-geostrophic columns (Fig. 7).

## V. DISCUSSION AND SUMMARY

In the limit of small Rossby and small Ekman numbers, the spin-up time in a cylinder with flat end walls is dictated by the so-called Ekman pumping, a flow normal to the boundary layer



of amplitude  $E^{1/2}$ . This pumping excites inertial modes in the bulk, which by advection will facilitate the transfer of angular momentum in and out of the boundary layer where the fluid is readjusted to the container azimuthal velocity. The spin-up time can be interpreted as the time it takes for the entire volume of fluid to circulate through the boundary layer, which yields  $\tau \propto E^{-1/2}$ . This mechanism exists in our experiment on the top flat end wall and will contribute to the re-synchronization of the fluid rotation; however, as we observed by varying the Ekman number, the scaling in the  $E^{1/2}$  characteristic of the purely viscous spin-up is altered as soon as we add topography.

In any container that does not have both the top and bottom wall smooth and perpendicular to the rotation axis, such as spherical shells, sliced cylinders, or cylinders with topography, the classical viscous meridional circulation is supplemented by an inviscid component  $\mathbf{u}_d = \mathbf{u} \cdot \nabla \mathbf{h}$  due to the deflection of the flow normal to the boundary, with  $h$  being the height of the column of water and  $\mathbf{u}$  being the local velocity. In our experiment, this supplemental pumping can be seen in our Kalliroscope visualization near the topography just after the tank is set to the new rotation rate (top row of Fig. 7). In contrast with the flat cylinder where the Ekman pumping drives large scale inertial modes in the interior, the influx induced by the topography will propagate in the interior in the form of inertial waves that have no preferential azimuthal wave number and a broad range of length scales due to the sharp edges of the blocks. As long as the initial influx exists, it will enhance the transport of angular momentum compared to the purely viscous pumping. This supports our observation that topography always leads to a shorter spin-up time. With  $\lambda_s = 1$  and  $\lambda_s = 0$  representing flat walls, we also expect the spin-up time to be minimal for a particular wavelength, as reported in this study.

Our results support a transport of the initial velocity perturbation induced by the topography through inertial waves for all wave numbers smaller than a critical value  $k_{max} \sim \varepsilon^{-1/2}$ . For larger wave numbers, the local non-linear interactions at those small scales transfer energy across the spectrum faster than they are transported by the inertial waves. For  $\lambda_s = 0.06$  (TOPO 08), the dynamics seem to be predominantly non-linear, as suggested by the absence of inertial wave propagation and a decay rate independent of the Ekman number, yet the spin-up is less efficient than for  $\lambda_s = 0.12$  (TOPO 16) where inertial waves are still a dominant feature of the flow.

The inherent difficulties due to the transient nature of the spin-up and the limited data make it difficult to draw a hard conclusion on what defines the optimal wavelength. Nevertheless, what seems to emerge from this study is that the spin-up with topography is governed by two competing mechanisms: on the one hand, inertial wave propagation, which could be increasingly efficient as the topography wavelength reduces; and on the other hand, non-linear effects transferring energy across scales, which seems to be less efficient at the conditions of our experiments. The limited range of accessible Rossby and Ekman numbers does not allow us to derive clear scaling laws for each topography. Yet, as the spin-up time increases with decreasing Ekman numbers for all but  $\lambda_s = 0.06$  (TOPO 08), the non-linear effects dominant for  $\lambda_s = 0.06$  (TOPO 08) at  $\varepsilon = 0.05$  should eventually be associated with the shortest

spin-up time at low enough  $E$ . Meanwhile, if the cutoff wave number defines the optimal wavelength, decreasing  $\varepsilon$  with all other parameters constant such that  $k_{TOPO08} < (H\varepsilon)^{-1/2}$  should also result in  $\lambda_s = 0.06$  (TOPO 08) in having shortest spin-up time. However, neither of these experiments could be performed with the actual device, indeed reducing  $\varepsilon$  leads to perturbations too small to be measurable and increasing  $H$  or the base rotation rate  $\Omega$  would require a complete rethinking of the experimental apparatus.

While the range of Ekman numbers covered in this study applies to typical industrial applications, it remains difficult to extrapolate our results in the context of planetary bodies. Further experiments should be conducted in this direction, in particular, considering the more realistic case of smooth topography such as bumps for which the gradient of topography remains finite. Finally we denote that the limiting case of a topography height of comparable or even smaller height than the Ekman boundary layer thickness is beyond the scope of this paper, but preliminary experiments suggest that it is governed by different mechanisms enhancing exchange of angular momentum in the boundary layer rather than an enhanced advection of angular momentum outside of the Ekman layer.

## ACKNOWLEDGMENTS

We thank Patrice Meunier, David Cebon, Nathanael Schaeffer, and Andrew Jackson for fruitful discussions. We would like to thank the reviewers for their pertinent comments from which this final version greatly benefited. This work is supported by ETH ZURICH Research Grant No. ETH-26 15-1.

- <sup>1</sup>T. Maxworthy, "Topographic effects in rapidly-rotating fluids: Flow over a transverse ridge," *Z. Angew. Math. Phys. ZAMP* **28**, 853–864 (1977).
- <sup>2</sup>J. G. Charney and J. G. DeVore, "Multiple flow equilibria in the atmosphere and blocking," *J. Atmos. Sci.* **36**, 1205–1216 (1979).
- <sup>3</sup>B. Legras and M. Ghil, "Persistent anomalies, blocking and variations in atmospheric predictability," *J. Atmos. Sci.* **42**, 433–471 (1985).
- <sup>4</sup>J.-O. Wolff, E. Maier-Reimer, and D. J. Olbers, "Wind-driven flow over topography in a zonal  $\beta$ -plane channel: A quasi-geostrophic model of the antarctic circumpolar current," *J. Phys. Oceanogr.* **21**, 236–264 (1991).
- <sup>5</sup>E. R. Weeks, Y. Tian, J. Urbach, K. Ide, H. L. Swinney, and M. Ghil, "Transitions between blocked and zonal flows in a rotating annulus with topography," *Science* **278**, 1598–1601 (1997).
- <sup>6</sup>Y. Tian, E. R. Weeks, K. Ide, J. Urbach, C. N. Baroud, M. Ghil, and H. L. Swinney, "Experimental and numerical studies of an eastward jet over topography," *J. Fluid Mech.* **438**, 129–157 (2001).
- <sup>7</sup>P. I. Bell and A. M. Soward, "The influence of surface topography on rotating convection," *J. Fluid Mech.* **313**, 147–180 (1996).
- <sup>8</sup>J. Herrmann and F. Busse, "Stationary and time dependent convection in the rotating cylindrical annulus with modulated height," *Phys. Fluids* **10**, 1611–1620 (1998).
- <sup>9</sup>T. von Larcher, A. Fournier, and R. Hollerbach, "The influence of a sloping bottom endwall on the linear stability in the thermally driven baroclinic annulus with a free surface," *Theor. Comput. Fluid Dyn.* **27**, 433–451 (2013).
- <sup>10</sup>M. Westerburg and F. Busse, "Centrifugally driven convection in the rotating cylindrical annulus with modulated boundaries," *Nonlinear Processes Geophys.* **10**, 275–280 (2003).
- <sup>11</sup>M. A. Calkins, J. Noir, J. D. Eldredge, and J. M. Aurnou, "The effects of boundary topography on convection in earth's core," *Geophys. J. Int.* **189**, 799–814 (2012).
- <sup>12</sup>H. Greenspan and L. Howard, "On a time-dependent motion of a rotating fluid," *J. Fluid Mech.* **17**, 385–404 (1963).

- <sup>13</sup>H. Greenspan, "On the general theory of contained rotating fluid motions," *J. Fluid Mech.* **22**, 449–462 (1965).
- <sup>14</sup>H. P. Greenspan, *The Theory of Rotating Fluids* (CUP, 1968).
- <sup>15</sup>E. Benton and A. Clark, Jr., "Spin-up," *Annu. Rev. Fluid Mech.* **6**, 257–280 (1974).
- <sup>16</sup>P. Duck and M. Foster, "Spin-up of homogeneous and stratified fluids," *Annu. Rev. Fluid Mech.* **33**, 231–263 (2001).
- <sup>17</sup>E. Wedemeyer, "The unsteady flow within a spinning cylinder," *J. Fluid Mech.* **20**, 383–399 (1964).
- <sup>18</sup>P. D. Weidman, "On the spin-up and spin-down of a rotating fluid. Part 1. Extending the Wedemeyer model," *J. Fluid Mech.* **77**, 685–708 (1976).
- <sup>19</sup>C. Kitchens, "Navier-Stokes solutions for spin-up in a filled cylinder," *AIAA J.* **18**, 929–934 (1980).
- <sup>20</sup>A. Warn-Varnas, W. W. Fowles, S. Piacsek, and S. M. Lee, "Numerical solutions and laser-Doppler measurements of spin-up," *J. Fluid Mech.* **85**, 609–639 (1978).
- <sup>21</sup>P. D. Weidman, "On the spin-up and spin-down of a rotating fluid. Part 2. Measurements and stability," *J. Fluid Mech.* **77**, 709–735 (1976).
- <sup>22</sup>J. Pedlosky and H. Greenspan, "A simple laboratory model for the oceanic circulation," *J. Fluid Mech.* **27**, 291–304 (1967).
- <sup>23</sup>J. Van De Konijnenberg, V. Naulin, J. J. Rasmussen, B. Stenum, and G. Van Heijst, "Linear spin-up in a sliced cylinder," *Geophys. Astrophys. Fluid Dyn.* **92**, 85–114 (2000).
- <sup>24</sup>G. J. F. V. Heijst, L. R. M. Maas, and C. W. M. Williams, "The spin-up of fluid in a rectangular container with sloping bottom," *J. Fluid Mech.* **265**, 125–159 (1994).
- <sup>25</sup>L. Li, M. D. Patterson, K. Zhang, and R. R. Kerswell, "Spin-up and spin-down in a half cone: A pathological situation or not?," *Phys. Fluids* **24**, 116601 (2012).
- <sup>26</sup>J. Van De Konijnenberg and G. Van Heijst, "Spin-up in a rectangular tank with a discontinuous topography," *Phys. Fluids* **8**, 2943–2952 (1996).
- <sup>27</sup>P. Matisse and M. Gorman, "Neutrally buoyant anisotropic particles for flow visualization," *Phys. Fluids* **27**, 759–760 (1984).
- <sup>28</sup>P. Meunier and T. Leweke, "Analysis and treatment of errors due to high velocity gradients in particle image velocimetry," *Exp. Fluids* **35**, 408–421 (2003).
- <sup>29</sup>O. M. Phillips, "Energy transfer in rotating fluids by reflection of inertial waves," *Phys. Fluids* **6**, 513 (1963).
- <sup>30</sup>I. Kolvin, K. Cohen, Y. Vardi, and E. Sharon, "Energy transfer by inertial waves during the buildup of turbulence in a rotating system," *Phys. Rev. Lett.* **102**, 014503 (2009).